

Slice imaging of nitric acid photodissociation: The O(¹D) + HONO channel

Nuradhika Herath, Stephanie C. Everhart, Arthur G. Suits, and Oleg S. Vasyuntinskii

Citation: *J. Chem. Phys.* **134**, 034311 (2011); doi: 10.1063/1.3540651

View online: <https://doi.org/10.1063/1.3540651>

View Table of Contents: <http://aip.scitation.org/toc/jcp/134/3>

Published by the [American Institute of Physics](#)

Articles you may be interested in

[UV Photodissociation Dynamics of Nitric Acid: The Hydroxyl Elimination Channel](#)

Chinese Journal of Chemical Physics **22**, 191 (2009); 10.1088/1674-0068/22/02/191-196

PHYSICS TODAY

WHITEPAPERS

ADVANCED LIGHT CURE ADHESIVES

Take a closer look at what these environmentally friendly adhesive systems can do

READ NOW

PRESENTED BY
 **MASTERBOND**
ADHESIVES | SEALANTS | COATINGS

Slice imaging of nitric acid photodissociation: The O(¹D) + HONO channel

Nuradhika Herath,¹ Stephanie C. Everhart,¹ Arthur G. Suits,^{1,a)} and Oleg S. Vasyuntinskii²

¹Department of Chemistry, Wayne State University, Detroit, Michigan 48202, USA

²Ioffe Physico-Technical Institute, Russian Academy of Sciences, 194021 St. Petersburg, Russia

(Received 24 August 2010; accepted 21 December 2010; published online 20 January 2011)

We report an imaging study of nitric acid (HNO₃) photodissociation near 204 nm with detection of O(¹D), one of the major decomposition products in this region. The images show structure reflecting the vibrational distribution of the HONO coproduct and significant angular anisotropy that varies with recoil speed. The images also show substantial alignment of the O(¹D) orbital, which is analyzed using an approximate treatment that reveals that the polarization is dominated by incoherent, high order contributions. The results offer additional insight into the dynamics of the dissociation of nitric acid through the S₃ (2 ¹A') excited state, resolving an inconsistency in previously reported angular distributions, and pointing the way to future studies of the angular momentum polarization. © 2011 American Institute of Physics. [doi:10.1063/1.3540651]

I. INTRODUCTION

The ultraviolet photodissociation of nitric acid is of considerable importance in Earth's atmosphere,¹ motivating many studies of its dissociation processes, branching ratios, and quantum yields.^{2–13} In recent years it has become clear that in the region of the intense deep UV absorption to the S₃ (2 ¹A') excited state at 190 nm, the products O(¹D) + HONO dominate over the OH + NO₂ (1 ²B₂) channel despite being energetically disfavored by 2 eV.¹³ There is some disagreement over the angular distributions, and the dynamical studies in this region have exclusively used photofragment translational spectroscopy (PTS), first by Huber and coworkers⁴ and later by the Butler group.⁹ This system is thus a promising one for application of the high-resolution dc slice imaging approach, as state-correlated product distributions may be used to gain deeper insight into the dissociation mechanisms and resolve some of these open questions.

The ground state of HNO₃ is planar, of ¹A' symmetry, and there is a weak transition at 260 nm accessing the S₁ (¹A'') state.¹⁴ This state exclusively dissociates to OH + NO₂, and it has been the subject of numerous studies.^{3,7,9} There is another ¹A'' state at 337 nm with little oscillator strength as well as the broad S₃ absorption mentioned above peaking at 190 nm.¹⁴ This transition is described by Bai and Segal as a mixture of nπ* and ππ* transitions. Although the ground state is planar, all of these excited singlet states possess similar pyramidal equilibrium geometries.¹⁴ Product branching at 193 nm was reported by Butler and coworkers⁹ based on analysis of the PTS results: they concluded total branching to O atom formation of 67%, with 54% to O (¹D) and the remainder to the ground state O (³P). Formation of OH + NO₂ accounted for the remaining 33%, including both ground state and electronically excited NO₂. There is rough agreement between these determinations and results from Ravishankara and coworkers³ who reported quantum yields for O(¹D) at 193 and 222 nm of 33% and 7%, respectively.

In this study, O(¹D) is sensitively probed via 2 + 1 resonant ionization at 205 nm (¹P₁ ←← ¹D₁) and 203 nm (¹F₃ ←← ¹D₁), allowing us to perform convenient “one-laser” (both dissociation and probe) imaging studies following excitation to the S₃ state.

II. EXPERIMENTAL

The detailed description of the experimental setup employing the dc slice imaging approach has been described previously^{15–17} and only a brief outline is given here. Fuming HNO₃ acid (99.5%, Sigma Aldrich) was bubbled with Ar to remove traces of NO₂. O(¹D) images from NO₂ were also recorded and compared to ensure that there was no residual contamination of the HNO₃ signal. Argon was then also used as a carrier gas to deliver 5% HNO₃ at a backing pressure of 2 bar into the source chamber operated at 10^{−5} Torr. A supersonic molecular beam of the resulting gas mixture was generated by expansion through a solenoid valve. This molecular beam entered the main chamber, held at 10^{−7} Torr, through a 1 mm skimmer. A linearly polarized laser intersects the molecular beam perpendicular to the propagation axis. The tunable UV laser beam was produced by the frequency doubling of the fundamental output of a dye laser (Spectra-Physics Sirah) pumped by the second harmonic of a Nd:YAG laser (Spectra-Physics Quanta-Ray PRO-250) in a potassium dihydrogen phosphate (KDP) crystal, then mixing the fundamental and doubled light in a beta-barium borate (BBO) crystal after matching the polarization using a waveplate. Dissociation of the HNO₃ and probing of the O(¹D) product were accomplished by a single laser beam, linearly polarized parallel to the detector face. The O (¹D) was probed by 2 + 1 REMPI through the ¹P₁ ←← ¹D₂ (205.4 nm) and ¹F₃ ←← ¹D₂ (203.8 nm) transitions. The output power of the laser was ~1.4 mJ. The laser frequency was continuously scanned across the Doppler profile during image acquisition. The resulting O⁺ ions were detected by a 120 mm microchannel detector (MCP) coupled to a fast

^{a)}Electronic mail: asuits@chem.wayne.edu.

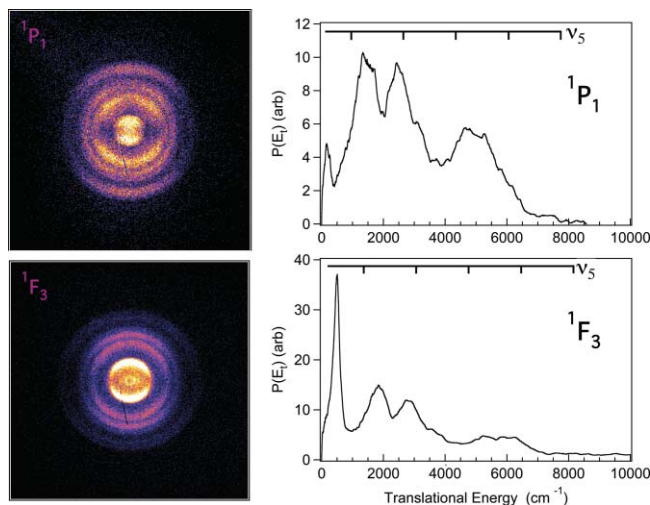


FIG. 1. dc sliced images and translational energy distributions of HNO_3 dissociation at 205.1 and 203.8 nm probed via the $\text{O}(^1\text{P}_1 \leftarrow ^1\text{D}_2)$ and $\text{O}(^1\text{F}_3 \leftarrow ^1\text{D}_2)$ transitions, respectively.

phosphor screen, where the gate of the time of flight was set to detect the mass of the O atom. For the dc slice imaging approach an ~ 60 ns gate was applied onto the MCP in order to select the center of the ion cloud. The phosphor screen was monitored by a CCD camera and a photomultiplier tube. Ion impact spots were centroided prior to integration. The imaging acquisition and analysis were done by our IMACQ megapixel imaging software as reported previously.¹⁸ dc sliced velocity images were calibrated by the detection of N_2 from the photodissociation of N_2O at 203.6 nm.¹⁹

III. RESULTS

dc slice images of photodissociation of HNO_3 obtained at 205.4 and 203.8 nm are shown in Fig. 1. Each image was acquired by averaging 100 000 shots. Images $^1\text{P}_1$ and $^1\text{F}_3$ were obtained by probing the $\text{O}(^1\text{D})$ atom via the $^1\text{P}_1 \leftarrow ^1\text{D}_2$ ($2 \times 48\,668.3\text{ cm}^{-1}$) and $^1\text{F}_3 \leftarrow ^1\text{D}_2$ ($2 \times 49\,064.2\text{ cm}^{-1}$) transitions, respectively. Both images consist of four rings showing a parallel transition. Figure 1 also shows the corresponding translational energy distributions obtained from the images. The translational energy plots show four peaks corresponding to distinct rings in the dc slice images. For $^1\text{P}_1$ and $^1\text{F}_3$ images, the position of each peak is roughly the same (there is only 400 cm^{-1} difference in available energy), but the relative intensities of each ring vary. In particular, the intensity of the sharp peak at low translational energy is significantly larger for HNO_3 dissociation at 203 nm ($^1\text{F}_3$ probe) than for dissociation at 205 nm ($^1\text{P}_1$ probe).

The images show additional structure beyond that expected for the scattering distribution following one-photon dissociation. This is clearly a manifestation of polarization of the $\text{O}(^1\text{D})$ orbital which modulates the detection efficiency, a $\mathbf{v} \cdot \mathbf{J}$ vector correlation. The angular momentum polarization of atomic products in photolysis of important atmospheric polyatomic molecules has been the subject of many recent publications.^{20–25}

It is most apparent on the second ring of the $^1\text{P}_1$ probe transition. Figure 2 shows the angular distributions obtained for each ring of the images. To understand the structure in these images, we consider the angular momentum distribution of $\text{O}(^1\text{D})$ from the photodissociation of HNO_3 molecules and its manifestation in these one-laser experiments. Given that the laser light source is linearly polarized parallel to the laboratory Z-axis, the expression for the experimental signal is²⁶

$$I_s = C \left[\rho_{00} + \frac{P_2}{P_0} \rho_{20} + \frac{P_4}{P_0} \rho_{40} \right], \quad (1)$$

where ρ_{K0} , $K = 0, 2, 4$, is the photofragment state multipole²⁷ and P_K is the two-photon line strength factor.²⁸ As shown earlier by Mo and Suzuki,²⁹ absolute line strength factors are difficult to obtain, but the relative values may be easily calculated for these transitions. For the transition $^1\text{F}_3 \leftarrow ^1\text{D}_2$ the ratios of the line strength factors are $P_2/P_0 = 0.68$ and $P_4/P_0 = -0.11$; for the $^1\text{P}_1 \leftarrow ^1\text{D}_2$ transition, they are -0.60 and -1.1 , respectively.^{28,29}

The expressions for the fragment state multipoles in Eq. (1) can be presented in the form³⁰

$$\begin{aligned} \rho_{00}(\theta, \phi) &= \frac{1}{4\pi\sqrt{2j_A+1}} [1 + \beta P_2(\cos \theta)], \\ \rho_{K0}(\theta, \phi) &= \frac{\sqrt{2K+1} V_K(j_A)}{4\pi\sqrt{2j_A+1}} \left\{ d_{00}^K(\theta)(s_K - 2\alpha_K P_2(\cos \theta)) \right. \\ &\quad \left. - \sqrt{6} \gamma_K d_{01}^K(\theta) \sin \theta \cos \theta - \frac{\sqrt{6}}{2} \eta_K d_{02}^K(\theta) \sin^2 \theta \right\}, \end{aligned} \quad (2)$$

where $P_2(\cos \theta)$ is the second order Legendre polynomial, $d_{00}^K(\theta)$ are Wigner d -functions, and the rank K can take the values $K = 2$ and $K = 4$. Note that these Legendre polynomials, with $\cos \theta$ arguments, are distinct from the line strength factors above.

The anisotropy parameters, α_K , s_K , γ_K , and η_K in Eq. (2), embody the full description of the orbital alignment that can be probed via a two-photon transition. In the case of photodissociation of a linear molecule in the absence of Coriolis interactions, the parameters α_K and s_K represent contributions to the photofragment alignment from incoherent excitation via perpendicular and parallel transitions, while the parameters γ_K and η_K represent contributions from coherent excitation.²⁸

In the more general case of photolysis of an arbitrary polyatomic molecule, the interpretation given above may not be strictly valid, because each of the parameters can contain contributions from incoherent parallel and perpendicular excitations as well as contributions from coherent excitations.^{31,32} However, as recently shown by Shternin and Vasyutinskii,³¹ the angular distributions in Eqs. (2) and (3) remain valid for any photolysis reaction. Each anisotropy parameter in Eq. (3) is proportional to a certain universal *anisotropy transforming coefficient* $\mathbf{c}_{k_d q}^K$, where K is the photofragment rank, $k_d = 0, 1, 2$ is the rank of the photolysis light polarization matrix, and q is the projection of each of the ranks K and k_d onto the *recoil* axis. The projection $q = \Omega - \Omega'$ labels the coherence between the helicity states Ω and Ω'

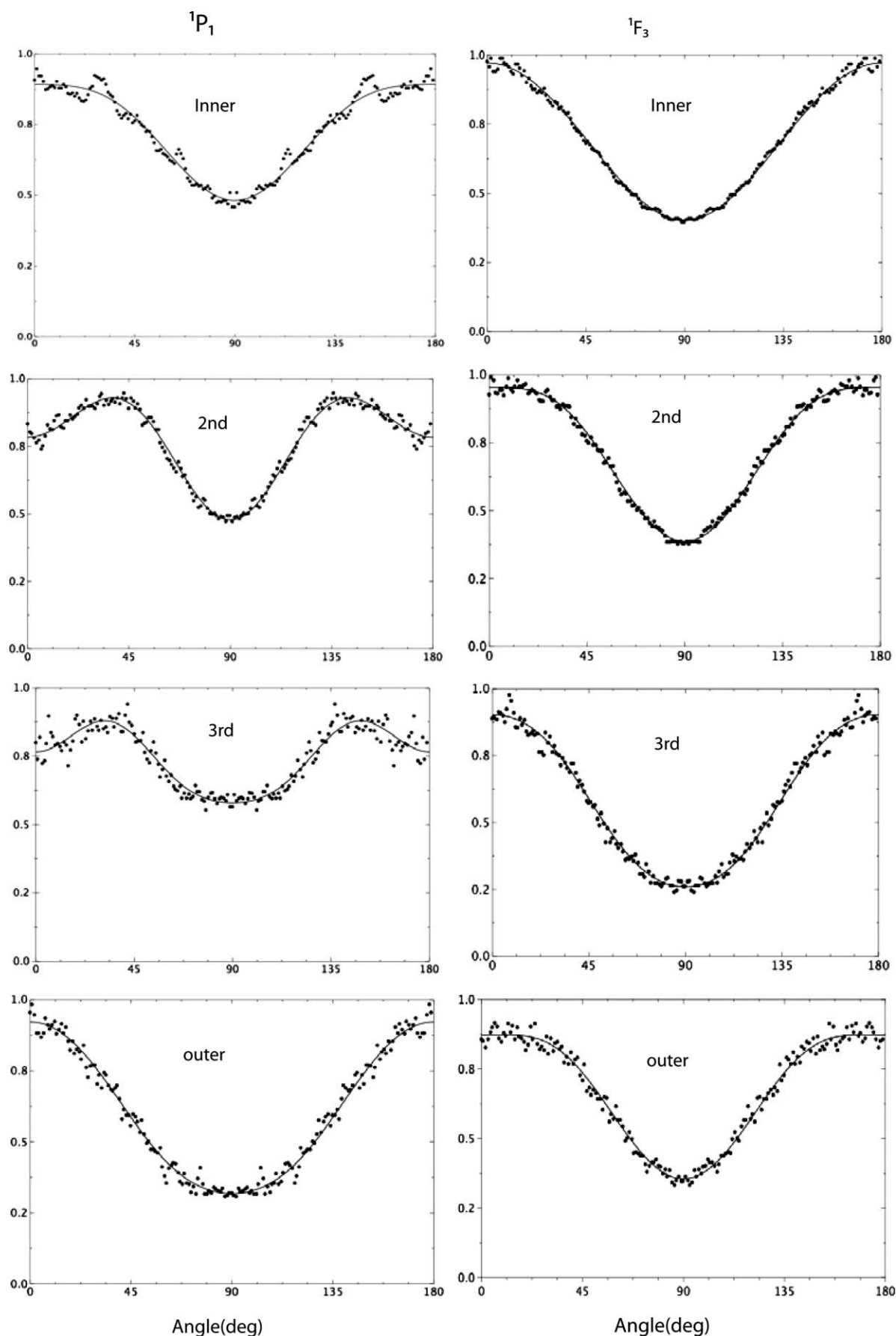


FIG. 2. Angular distributions of the O(¹D) recoil velocity from the ~ 204 nm photodissociation of HNO₃ for each of the four rings in the images in Fig. 1 obtained via the ¹F₃ ← ¹D₂ and ¹P₁ ← ¹D₂ oxygen transitions. The smooth curves denote the fit of Eq. (6) to experimental data.

of the product angular momentum onto the recoil axis. In particular, $\mathbf{c}_{20}^2 = -\sqrt{30} V_2(j_A)\alpha_2$, $\mathbf{c}_{00}^2 = -\sqrt{15} V_2(j_A)s_2$, $\mathbf{c}_{21}^2 = -\sqrt{15/2} V_2(j_A)\gamma_2$, and $\mathbf{c}_{22}^2 = -\sqrt{15/2} V_2(j_A)\eta_2$. Moreover, Shternin and Vasyutinskii have proved³¹ that the *coherent quantum number* $q = 0, \pm 1, \pm 2$ is a constant of motion, which is preserved in the photolysis of any polyatomic molecule, irrespective of the reaction mechanism.

Usually the anisotropy parameters are determined in imaging experiments by recording images in several exper-

imental geometries to isolate particular contributions.²⁸ In these one-beam experiments, this is not possible, so we develop an approximate treatment to examine the dominant features. A more detailed study of the O(¹D) polarization will follow in a future publication.

Substituting Eqs. (2) and (3) into Eq. (1), the latter can be rewritten as

$$I_s = C' \left[1 + \beta P_2(\cos \theta) + \frac{\sqrt{5}P_2}{P_0} V_2(j_A) P_2(\cos \theta) [s_2 - 2\alpha_2 P_2(\cos \theta)] + \frac{3P_4}{P_0} V_4(j_A) P_4(\cos \theta) \right. \\ \times [s_4 - 2\alpha_4 P_2(\cos \theta)] - \frac{3\sqrt{5}P_2}{P_0} V_2(j_A) \gamma_2 \sin^2 \theta \cos^2 \theta - \frac{3\sqrt{5}P_2}{4P_0} V_2(j_A) \eta_2 \sin^4 \theta \\ \left. + \frac{3\sqrt{30}P_4}{4P_0} V_4(j_A) \gamma_4 \sin^2 \theta \cos^2 \theta (3 - 7 \cos^2 \theta) + \frac{3\sqrt{15}P_4}{8P_0} V_4(j_A) \eta_4 \sin^4 \theta (1 - 7 \cos^2 \theta) \right]. \quad (4)$$

Expansion over the Legendre polynomials gives

$$I_s = C' \left[1 - \frac{2\sqrt{5}}{5} \frac{P_2}{P_0} V_2(\alpha_2 + \gamma_2 + \eta_2) + \left(\beta + \frac{2\sqrt{5}}{7P_0} P_2 \left(\frac{7}{2}s_2 - 2\alpha_2 - \gamma_2 + 2\eta_2 \right) \right. \right. \\ \left. \left. - \frac{2P_4}{7P_0} V_4(6\alpha_4 + \sqrt{30}\gamma_4 + \sqrt{15}\eta_4) \right) P_2(\cos \theta) - \left(\frac{9\sqrt{5}}{35} \frac{P_2}{P_0} V_2 \left(4\alpha_2 - \frac{8}{3}\gamma_2 + \frac{2}{3}\eta_2 \right) \right. \right. \\ \left. \left. - \frac{3P_4}{P_0} V_4 \left(s_4 - \frac{40}{77}\alpha_4 - \frac{2\sqrt{30}}{77}\gamma_4 + \frac{12\sqrt{15}}{77}\eta_4 \right) \right) P_4(\cos \theta) - \frac{2P_4}{11P_0} V_4(15\alpha_4 - 2\sqrt{30}\gamma_4 + \sqrt{15}\eta_4) P_6(\cos \theta) \right]. \quad (5)$$

Equation (5) shows that in general the experimental signal can be presented in the known form

$$I_s \propto 1 + \beta_2 P_2(\cos \theta) + \beta_4 P_4(\cos \theta) + \beta_6 P_6(\cos \theta), \quad (6)$$

where the fitting parameters β_2 , β_4 , and β_6 refer to the anisotropy parameters according to Eq. (5).

A fit of Eq. (6) to the angular distributions shown in Fig. 2 furnishes optimized values for β_2 , β_4 , and β_6 , shown in Table I. Note that the second term in the first line in the rhs in Eq. (5) is proportional to the total photofragment alignment averaged over all recoil angles, which is usually small in photolysis of polyatomic molecules.²⁶

Neglecting the second term in the first line in the rhs in Eq. (5) compared with the unity, the relationship between the β_2 , β_4 , and β_6 parameters in Eq. (6) and the

anisotropy parameters β , α_2 , α_4 , s_2 , and s_4 in Eqs. (5) can be presented as

$$\beta_2 = \beta + \frac{2\sqrt{5}}{7P_0} P_2 \left(\frac{7}{2}s_2 - 2\alpha_2 - \gamma_2 + 2\eta_2 \right) - \frac{2P_4}{7P_0} V_4(6\alpha_4 + \sqrt{30}\gamma_4 + \sqrt{15}\eta_4), \quad (7)$$

$$\beta_4 = -\frac{9\sqrt{5}}{35} \frac{P_2}{P_0} V_2 \left(4\alpha_2 - \frac{8}{3}\gamma_2 + \frac{2}{3}\eta_2 \right) + \frac{3P_4}{P_0} V_4 \left(s_4 - \frac{40}{77}\alpha_4 - \frac{2\sqrt{30}}{77}\gamma_4 + \frac{12\sqrt{15}}{77}\eta_4 \right), \quad (8)$$

$$\beta_6 = -\frac{2P_4}{11P_0} V_4(15\alpha_4 - 2\sqrt{30}\gamma_4 + \sqrt{15}\eta_4). \quad (9)$$

The resulting six equations arising from the $^1F_3 \leftarrow ^1D_2$ and $^1P_1 \leftarrow ^1D_2$ transitions contain nine unknown anisotropy parameters and therefore cannot be resolved in general within the condition of our one-laser experiment. However, an approximate treatment of the problem is possible and given in Sec. IV.

TABLE I. Fitted β parameters shown in Fig. 2.

	1P_1			1F_3		
	β_2	β_4	β_6	β_2	β_4	β_6
Inner	0.43	-0.18	0.01	0.60	0.00	0.00
2nd	0.43	-0.34	0.00	0.56	-0.24	-0.03
3rd	0.41	-0.14	-0.08	0.96	-0.05	-0.03
Outer	1.04	0.14	-0.10	0.75	-0.26	-0.02

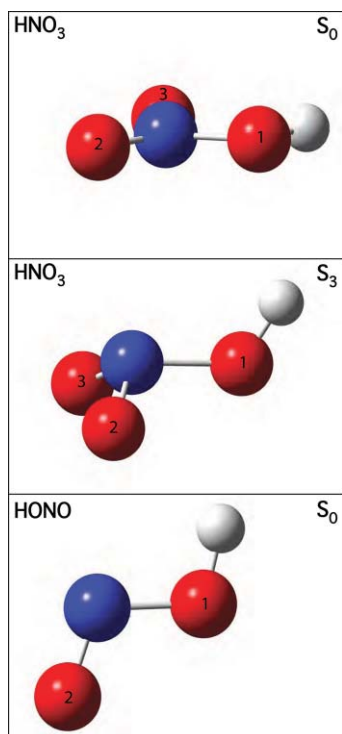


FIG. 3. The geometries of HNO₃ ground state, excited state (S₃), and *trans*-HONO.

IV. DISCUSSION

We begin our discussion of these results with an examination of the translational energy distributions, after which we will turn to the angular distributions and orbital polarization. The structure observed in the total translational energy distributions, shown in Fig. 1, is due to the vibrational excitation of the HONO coproduct; the lowest electronic excitation of HONO is inaccessible.³³ HONO exists in two isomeric forms, *cis* and *trans*, with the *trans* isomer 200 cm⁻¹ lower in energy and a barrier of 3500 cm⁻¹ separating them.³⁴ *Ab initio* calculations by Bai and Segal¹⁴ reported the molecular geometry of the S₃ excited state of nitric acid as pyramidal, with NO bonds bent 30° below the N–OH bond, and the O–H bond rotated 90° above the molecular plane, as depicted in Fig. 3. This suggests a HONO product that is predominantly *trans*, and therefore we will focus our attention on this isomer, although the vibrational frequencies are quite similar for both HONO species.

There are six vibrational modes in *trans*-HONO, and their frequencies and character are presented in Table II. It

TABLE II. Vibrational frequencies of HONO (Ref. 33).

Vibrational frequency (cm ⁻¹)	Vibrational excitation	
544	ν_1	$\tau(\text{O–H})$
598	ν_2	$\delta(\text{ONO})$
793	ν_3	$\sigma(\text{O–H})$
1263	ν_4	$\delta(\text{NOH})$
1698	ν_5	$\sigma(\text{N=O})$
3590	ν_6	$\sigma(\text{O–H})$

TABLE III. Geometries of HNO₃ and *trans*-HONO. Bond lengths in Å and angles in degrees.

	R _{OH}	R _{NO}	R _{NO₂}	O ₁ NO ₂	O ₂ NO ₃	HO ₁ N
HNO ₃ S ₀ (1 ¹ A')	0.95	1.39	1.22	115.0	130.0	102.0 ^a
HNO ₃ S ₃ (2 ¹ A')	0.95	1.47	1.30	108.6	112.8	103.3 ^a
<i>t</i> -HONO	0.96	1.43	1.17	110.7	...	103.0 ^b

^aReference 14.

^bReference 33.

is clear that there are too many possible modes and combinations to make unique fits to the four broad peaks we observe. To understand the likely vibrational excitation in the HONO coproduct, we thus consider the relations between the starting equilibrium geometry, the excited state geometry, and the HONO product, to look for large changes during the excitation and dissociation process. Table III shows the comparison of the molecular geometries of ground state HNO₃ (1¹A'), S₃ excited state HNO₃ (2¹A'), and *t*-HONO.^{33,35} Changes in N–O bond length and O–N–O bond angle are the major geometric adjustments to occur during the excitation from the ground state to the S₃ excited state and subsequent formation of *t*-HONO. The N–O bond length increases during the excitation and then decreases to a shorter length than in the ground state. This suggests significant excitation in the N=O stretching mode. Change in the O–N–O bond angle from 115° to 108.6° during S₃ ← S₀ excitation and then back to 110° in ground-state *t*-HONO likely induces excitation of the O–N–O bend. This, in conjunction with excitation to the pyramidal S₃ state in HNO₃ prior to dissociation, excites movement primarily in three main vibrational modes: the OH out of plane twist (ν_1), O–N–O bend (ν_2) and N=O stretching (ν_5). Therefore, neglecting possible exit channel dynamics, the translational energy distributions likely reflect excitation of these three dominant vibrational modes. According to the vibrational frequencies of *t*-HONO given in Table II, the difference between ν_1 and ν_2 is about 50 cm⁻¹. Thus the combination bands arising from vibrations of ν_1 and ν_2 cannot be distinguished separately. Furthermore $2\nu_1 + \nu_2$ is roughly equal to one quanta of ν_5 . Therefore we are unable to make unambiguous assignment for each peak of the translational energy distribution. However, in Fig. 1 we overlay the ν_5 vibrational mode spacings, as we expect this to be the dominant high frequency excitation, with low frequency combinations superimposed on this.

We note that the vibrational energy in HONO corresponding to the sharp low energy peak O(¹D) translational energy distribution is greater than four quanta of ν_5 . This peak is particularly interesting in that it is so sharp, and it grows so quickly with the modest increase in excitation energy. The intensity of this peak is quite consistent despite fluctuations in laser power, so we do not believe it to be associated with multiphoton dissociation. Furthermore, the similarity in the β value determined for this peak, discussed below, is quite consistent with others, again providing evidence that it is simply a HONO vibrational peak that has a strong dependence on excitation energy. Although our results provide no direct insight into the rotational excitation of HONO, it is likely to be significant, particularly for the faster HONO product, given the

TABLE IV. Fitted anisotropy parameters for each of the four rings in the images. Uncertainties are 2σ based on separate fits to several data sets.

	Inner	2nd	3rd	Outer
β	0.48(15)	0.47(9)	0.64(7)	0.84(12)
s_4	0.08(14)	0.24(5)	0.08(4)	0.04(14)
$(7/2 s_2 - 2\alpha_2 - \gamma_2 + 2\eta_2)$	0.11(20)	0.08(14)	0.36(22)	-0.19(30)
$(4\alpha_2 - 8/3\gamma_2 + 2/3\eta_2)$	0.01(1)	-0.12(4)	-0.04(6)	-0.17(8)
α_2	0.002(8)	-0.029(10)	-0.010(16)	-0.042(20)
s_2	0.40(90)	0.10(70)	1.2(12)	-1.0(16)

impulsive recoil, large bending excitation expected, and finite exit impact parameter. Future trajectory studies would be very useful to investigate this and to understand the detailed origin of this distinct vibrational structure we observe.

We now consider the β parameter values and the $O(^1D)$ orbital polarization. The fits to the angular distributions in Table I show that the terms related with β_6 give only a minor contribution to the signals observed for both the $^1F_3 \leftarrow ^1D_2$ and $^1P_1 \leftarrow ^1D_2$ probe transitions. Moreover, the corresponding β_6 values are quite small. Therefore, we neglected all anisotropy parameters α_4 , γ_4 , and η_4 in Eqs. (7)–(9) in the following analysis. The simplified Eqs. (7) and (8) were solved for the $^1F_3 \leftarrow ^1D_2$ and $^1P_1 \leftarrow ^1D_2$ transitions giving the parameters β , s_4 and the parameter combinations $(\frac{7}{2}s_2 - 2\alpha_2 - \gamma_2 + 2\eta_2)$, $(4\alpha_2 - \frac{8}{3}\gamma_2 + \frac{2}{3}\eta_2)$ shown in Table IV.

The β values show a significant recoil velocity dependence and vary from 0.47 to 0.84, with the faster $O(^1D)$ product having the larger β anisotropy parameter. These values are significantly lower than the 1.4 value measured by the Butler group,⁹ although they compare favorably with $\beta = 0.6$ reported by Felder *et al.*⁴ It seems that in the Butler study, they focused on the faster O atom product to avoid possible contamination from clusters, and this may have contributed to the greater anisotropy observed.

In the axial recoil limit, a theoretical anisotropy parameter β can be calculated based on the angle φ between the transition dipole moment μ and the recoil velocity \mathbf{v} : $\beta = 2P_2(\cos \varphi)$.³⁶ In the case of HNO_3 , μ lies in the molecular plane, parallel to the terminal oxygens.⁹ Assuming prompt dissociation from the ground state and recoil along the bond axis, $\varphi = 25^\circ$ determined from the geometry reported in Table III gives a theoretical $\beta = 1.47$, as reported by Butler's group.⁹ For the pyramidal S_3 excited state equilibrium geometry, the analogous calculation gives a predicted β value of 0.98, still significantly more anisotropic than that we observe and reported by Huber. Back-calculation of the β 's reported here corresponds to $\text{O}_2\text{--N--O}_3$ bond angles of $91^\circ\text{--}99^\circ$, in contrast to the 130° in the ground state and 112.8° in the S_3 excited state. We suggest that the N=O bond cleavage occurs when the O--N--O bending excitation has overshoot the S_3 equilibrium geometry, and the extent of bending excitation, reduced translational energy, and lowered anisotropy, are all correlated.

Table IV reports the anisotropy parameters s_4 and the parameter combinations $(\frac{7}{2}s_2 - 2\alpha_2 - \gamma_2 + 2\eta_2)$, $(4\alpha_2$

$-\frac{8}{3}\gamma_2 + \frac{2}{3}\eta_2)$ as calculated using both the $^1F_3 \leftarrow ^1D_2$ and $^1P_1 \leftarrow ^1D_2$ transitions according to Eqs. (7) and (8) and the data in Table I. The contribution from the s_4 alignment mechanism seems to be significant in our experiment, in particular for the second ring in the images. The obtained s_4 -values can be compared with that obtained for N_2O photodissociation³⁰ [$s_4 = (9 \pm 2) \times 10^{-3}$] and with the possible physical range²⁶ ($s_4 = -1/5 \dots 1/5$). Direct determination of the parameters s_2 , α_2 , γ_2 , and η_2 from the parameter combinations above is not possible for a one-laser experiment and needs further approximations.

Here we assume that the contribution from the “coherent” parameters γ_2 and η_2 can be neglected as they do not appear to contribute significantly to the experimental images in Fig. 1. In that case, the parameters α_2 and s_2 can be easily obtained, and their values are also given in Table IV. It is clearly seen from Table IV that the anisotropy parameter α_2 has its value close to zero, while the anisotropy parameters s_2 (and s_4) are significant, although the uncertainty in the determined s_2 parameters is large. Note that both α_K and s_K anisotropy parameters refer to the contribution to the photofragment angular momentum alignment from incoherent ($q = 0$) mechanisms. The difference between these two sets of parameters is that α_K refers to the alignment which does not vanish after averaging over all recoil angles, while s_K refers to the alignment which exists only in the molecular frame and vanishes after averaging over all recoil angles.^{26,28} Moreover, $\alpha_K \propto \mathbf{c}_{20}^K$ and $s_K \propto \mathbf{c}_{00}^K$,³¹ which means that α_K refers to the *alignment of the photolysis light polarization vector* \mathbf{e} , while s_K refers to the *isotropic part of the photolysis light* and therefore reflect only the anisotropy of the intermolecular interactions during the photolysis.

The dominant contribution from the s_K alignment mechanism seems to be usual in the photodissociation of polyatomic molecules, where the alignment usually exists in the molecular frame and vanishes after averaging over all recoil angles.²⁶ In addition, upon examining the s_K terms we see the alignment related to the higher order $K = 4$ term is important for certain rings in the images in Fig. 1, which is particularly apparent in the image obtained through the 1P_1 probe as a result of the larger P_4/P_0 line strength factor compared to the 1F_3 transition. We emphasize, however, that the conclusion about the minor role of the “coherent” photodissociation mechanism related to the parameters γ_K and η_K is tentative and should be proved in the future using a two-laser experimental scheme.

Much of the study of the photodissociation of HNO_3 has focused on the $\text{OH} + \text{NO}_2$ channel.^{7,8,37,38} The dominant channel for the photodissociation of HNO_3 at 193 nm, however, is $\text{O} + \text{HONO}$ with quantum yields of 0.67.^{4,9} Recently Nonella *et al.*¹³ studied the wavepacket dynamics of HNO_3 in a two-dimensional treatment fixed in the planar geometry. A key interest in the work was accounting for the remarkable preference for $O(^1D)$ production despite the presence of a much lower energy, barrierless process forming $\text{OH} + \text{NO}_2$. They found that on the S_3 potential energy surface about 60% of the products form $O(^1D) + \text{HONO}$, and the reason is a much steeper slope of the potential along that dimension. It will be very interesting to see how these trends are manifested in a full-dimensional treatment, which is clearly called for

based on the angular distributions and vibrational excitation we observe.

V. CONCLUSION

Here we report the translational energy and angular momentum distributions of the $O(^1D)$ product from HNO_3 photodissociation near 204 nm. The vibrational energy distribution of the HONO coproduct, as seen through the $O(^1D)$ translational energy distribution, shows significant vibrational energy remaining in the molecule. Analysis of the angular distributions from both the $^1F_3 \leftarrow ^1D_2$ and $^1P_1 \leftarrow ^1D_2$ oxygen atom probe transitions resulted in an $O(^1D)$ recoil velocity-dependent β values of 0.47–0.84. Substantial alignment of the $O(^1D)$ orbital was observed and analyzed using an approximate treatment demonstrating that the polarization is dominated by incoherent, high order contributions.

ACKNOWLEDGMENTS

The authors thank Dr. Peter Shternin for useful discussions. This work was supported by the National Science Foundation (NSF) under Award No. CHE-0715300. O.S.V. appreciates support from the Russian Foundation for Basic Researches, Grant No. 08-03-00601-a.

- ¹J. Mettews, A. Sinha, and J. Francisco, *Proc. Natl. Acad. Sci. U.S.A.* **102**, 7449 (2005).
- ²A. Sinha, R. L. Vanderwal, and F. F. Crim, *J. Chem. Phys.* **91**, 2929 (1989).
- ³A. A. Turnipseed, G. L. Vaghjiani, J. E. Thompson, and A. R. Ravishankara, *J. Chem. Phys.* **96**, 5887 (1992).
- ⁴P. Felder, X. F. Yang, and J. R. Huber, *Chem. Phys. Lett.* **215**, 221 (1993).
- ⁵A. Schiffman, D. D. Nelson, and D. J. Nesbitt, *J. Chem. Phys.* **98**, 6935 (1993).
- ⁶J. R. Huber, *ChemPhysChem* **5**, 1663 (2004).
- ⁷F. Y. Wang, Z. C. Chen, Y. W. Zhang, Q. Shuai, B. Jiang, D. X. Dai, X. Y. Wang, and X. M. Yang, *Chin. J. Chem. Phys.* **22**, 191 (2009).
- ⁸F. Assenmacher, M. Gutmann, F. Noack, V. Stert, and W. Radloff, *Appl. Phys. B: Lasers Opt.* **71**, 385 (2000).
- ⁹T. Myers, N. Forde, B. Hu, D. Kitchen, and L. Butler, *J. Chem. Phys.* **107**, 5361 (1997).
- ¹⁰P. S. Yeh, G. H. Leu, Y. P. Lee, and I. C. Chen, *J. Chem. Phys.* **103**, 4879 (1995).
- ¹¹Q. Li, R. Carter, and J. Huber, *Chem. Phys. Lett.* **334**, 39 (2001).
- ¹²M. Krisch, M. Reid, L. McCunn, L. Butler, and J. Shu, *Chem. Phys. Lett.* **397**, 21 (2004).
- ¹³M. Nonella, H. U. Suter, and J. R. Huber, *Chem. Phys. Lett.* **487**, 28 (2010).
- ¹⁴Y. Y. Bai and G. A. Segal, *J. Chem. Phys.* **92**, 7479 (1990).
- ¹⁵D. W. Chandler and P. L. Houston, *J. Chem. Phys.* **87**, 1445 (1987).
- ¹⁶A. T. J. B. Eppink and D. H. Parker, *Rev. Sci. Instrum.* **68**, 3477 (1997).
- ¹⁷D. Townsend, M. Minitti, and A. Suits, *Rev. Sci. Instrum.* **74**, 2530 (2003).
- ¹⁸W. Li, S. Chambreau, S. Lahankar, and A. Suits, *Rev. Sci. Instrum.* **76**, 63106 (2005).
- ¹⁹D. Neyer, A. Heck, and D. Chandler, *J. Chem. Phys.* **110**, 3411 (1999).
- ²⁰Y. Mo, H. Katayanagi, M. Heaven, and T. Suzuki, *Phys. Rev. Lett.* **77**, 830 (1996).
- ²¹Z. H. Kim, A. J. Alexander, and R. N. Zare, *J. Phys. Chem. A* **103**, 10144 (1999).
- ²²T. M. Teule, G. C. Groenenboom, D. W. Neyer, D. W. Chandler, and M. H. M. Janssen, *Chem. Phys. Lett.* **320**, 177 (2000).
- ²³S. K. Lee, D. Townsend, O. S. Vasyutinskii, and A. G. Suits, *Phys. Chem. Chem. Phys.* **7**, 1650 (2005).
- ²⁴A. J. van den Brom, T. P. Rakitzis, and M. H. M. Janssen, *J. Chem. Phys.* **123**, 164313 (2005).
- ²⁵M. Brouard, R. Cireasa, A. P. Clark, G. C. Groenenboom, G. Hancock, S. J. Horrocks, F. Quadri, G. A. D. Ritchie, and C. Vallance, *J. Chem. Phys.* **125** (2006).
- ²⁶A. G. Suits and O. S. Vasyutinskii, *Chem. Rev.* **108**, 3706 (2008).
- ²⁷A. Bracker, E. Wouters, A. Suits, and O. Vasyutinskii, *J. Chem. Phys.* **110**, 6749 (1999).
- ²⁸E. R. Wouters, M. Ahmed, D. S. Peterka, A. S. Bracker, A. G. Suits, and O. S. Vasyutinskii, in *Imaging in Chemical Dynamics*, edited by A. G. Suits and R. E. Continetti (American Chemical Society, Washington, DC, 2000), pp. 238–284.
- ²⁹Y. Mo and T. J. Suzuki, *J. Chem. Phys.* **112**, 3463 (2000).
- ³⁰A. G. Smolin, O. S. Vasyutinskii, E. R. Wouters, and A. G. Suits, *J. Chem. Phys.* **121**, 6759 (2004).
- ³¹P. S. Shternin and O. S. Vasyutinskii, *J. Chem. Phys.* **128**, 194314 (2008).
- ³²V. V. Kuznetsov, P. S. Shternin, and O. S. Vasyutinskii, *J. Chem. Phys.* **130**, 134312 (2009).
- ³³G. W. King and D. Moule, *Can. J. Chem.* **40**, 2057 (1964).
- ³⁴P. Dehayem-Kamadjeu, J. Orphal, I. Kleiner, and P. Flaud, *J. Mol. Spectrosc.* **234**, 182 (2005).
- ³⁵S. Y. Yu, C. G. Zhang, and M. B. Huang, *Chem. Phys. Lett.* **440**, 187 (2007).
- ³⁶R. N. Zare, *Mol. Photochem.* **4**, 1 (1972).
- ³⁷S. Baek, C. Park, and H. Kim, *J. Photochem. Photobiol., A* **104**, 13 (1997).
- ³⁸Y. Miller, G. Chaban, B. Finlayson-Pitts, and R. Gerber, *J. Phys. Chem. A* **110**, 5342 (2006).